Acta Materialia 206 (2021) 116598

Contents lists available at ScienceDirect

Acta Materialia

journal homepage: www.elsevier.com/locate/actamat

Radiation damage and thermal annealing in tunnel structured hollandite materials

Mingyang Zhao[a], Eric O'Quinn[b], Nancy Birkner[a], Yun Xu[a], Maik Lang[b], Kyle Brinkman[a,*]

[a] Department of Materials Science and Engineering, Clemson University, Clemson, SC 29634, USA
[b] Department of Nuclear Engineering, University of Tennessee, Knoxville, TN 37996, USA

ARTICLE INFO

Article history:
Received 31 August 2020
Revised 1 December 2020
Accepted 19 December 2020
Available online 30 December 2020

Keywords:
Hollandite
Radiation damage
Neutron total scattering
Calorimetry
Thermal annealing

ABSTRACT

Three tunnel structured hollandite samples ($Cs_{1.33}Ga_{1.33}Ti_{6.67}O_{16}$, $Cs_{1.33}Fe_{1.33}Ti_{6.67}O_{16}$, and $Cs_{1.33}Zn_{0.67}Ti_{7.33}O_{16}$) with demonstrated thermodynamic stability and chemical durability were synthesized and irradiated by a 1.1 GeV Au ion beam in order to study effects of B-site dopants on radiation stability. A crystalline-to-amorphous transformation induced by the high-energy ion irradiation was confirmed by complementary characterization techniques sensitive to different length-scales, such as powder X-ray diffraction, Raman spectroscopy and neutron total scattering. High-temperature oxide melt solution calorimetry was performed to determine the energy landscape before and after ion irradiation. Together, structural and thermodynamic analyses demonstrated distinctly different radiation responses of the hollandite with different B-site dopants; the Ga-substituted hollandite exhibited the smallest enthalpy of damage indicating the best radiation stability among the three samples. The hypothesized origin of the different radiation responses is the structural feature in the binary oxide form of the respective B-site dopants (e.g., Ga_2O_3 *versus* Fe_2O_3/ZnO for Ga and Fe/Zn dopants, respectively). Moreover, thermal analysis (i.e., differential scanning calorimetry) was conducted to investigate structural changes from the irradiation induced damaged states after thermal annealing. Results of thermal analysis revealed that the annealing-induced structural evolution of the radiation damaged hollandite structure is complex and decoupled at different length-scales. The long-range periodic structure (nanometers) was not recovered after thermal annealing and structural changes over a shorter range ($\leq \sim 3$ Å) occurred in multiple steps during the annealing process.

1. Introduction

Since the 1980s, substantial efforts have been devoted to investigations on the separation of long-lived fission products from waste streams, as well as the development of robust host matrices called "waste forms" for the incorporation of separated fission products [1-3]. Among a wide variety of radionuclides in waste streams, cesium (Cs) is one of the most problematic radionuclides to immobilize due to various issues [4], such as easy formation of water-soluble compounds during sintering, high volatility at elevated temperature, the large heat release from ^{137}Cs, and the long half-life of ^{135}Cs. Numerous studies have confirmed that hollandite is a promising candidate for Cs immobilization as it has superior chemical durability, thermal and structural stability, and radiation-damage resistance [5-12]. Hollandite has the general formula $A_xB_8O_{16}$ ($0 \leq x \leq 2$), where A can be monovalent and divalent cations (e.g., Cs^+ and Ba^{2+}) and the B-site cations can have valences between 2 and 4 (e.g., Zn^{2+}, Al^{3+}, Fe^{3+}, Ga^{3+}, Ti^{4+}, etc.) [7,8,10,13,14]. The structure of hollandite consists of double chains of edge-linked BO_6 octahedra which are connected to other double chains of BO_6 octahedra at corners to form a framework with large tunnels where the A-site cations are occupied [15]. Either monoclinic ($I2/m$) or tetragonal ($I4/m$) crystal structures can be adopted by hollandite depending on the relative sizes of cations on the A-sites and B-sites [14,16]. Significant effects of Cs content on thermodynamic stability [7,8,14], chemical durabilty [7,8,14] and radiation stability [17] have been reported in literature. However, the underlying mechanisms of radiation-resistance and potential recovery via thermal annealing have not been systematically studied for high Cs-containing hollandite compounds with different B-site dopants.

Heavy ion irradiations in the MeV energy range (e.g., Xe, Kr) are often used to simulate radiation damage induced by alpha-decay effects. Ion-beam experiments can create very high doses in short time periods to damage waste forms by using laboratory-based particle accelerators, so that one can analyze their response

* Corresponding author.
E-mail address: ksbrink@clemson.edu (K. Brinkman).

https://doi.org/10.1016/j.actamat.2020.116598
1359-6454/

in extreme radiation environments [17-21]. Although waste forms can be amorphized under such conditions, this amorphization is typically inhomogeneous and only occurs at the surface (in the sub-micron scale) due to the relatively low kinetic energies [17,20]. However, ion energies in the GeV range have recently become accessible with the advent of large ion accelerator facilities. The penetration depth of such swift heavy ions is much larger (~100 μm) than that of conventional keV-MeV ion beams, providing larger volumes of amorphous materials available for bulk characterization [22]. Moreover, it has been confirmed that the induced structural modifications are in some materials very similar for both GeV and keV-MeV ions [23].

In order to comprehensively analyze the structural evolution induced by irradiation, both long-range and short-range characterization before and after damage are essential. For example, powder X-ray diffraction (XRD) can be utilized to study long-range structure that reflects periodic crystalline assignments of hollandite unit cells, while neutron total scattering with pair distribution function (PDF) analysis and Raman spectroscopy are able to provide structural information at the short-range (typically $\leq$ ~10 Å) associated with various local bonding environments [12,24]. Neutron total scattering, in particular, is essential in probing the structural response of the anion sublattice to radiation due to the sensitivity of neutrons to oxygen [23].

Bulk thermodynamic measurements such as high-temperature oxide melt solution calorimetry has been applied to directly compare the energetic difference between unirradiated and irradiated samples by measuring enthalpies of drop solution in pyrochlore structured material systems such as $Dy_2Ti_2O_7$ [24]. In addition to quantifying the radiation damage in waste forms after ion irradiation, defect recovery pathways and defect dynamics help to better understand the stability of a waste form material under ion irradiation. Differential scanning calorimetry (DSC) can capture heat effects from damaged samples during heat treatment providing thermodynamic as well as kinetic information related to defect recovery. Previous combined structural and thermodynamic studies on ion irradiated pyrochlore showed that radiation damage formation and recovery is in these relatively simple structured oxide materials more complex than previously thought with distinct processes across different length-scales [24]. This motivated similar studies on more complicated tunnel structured oxide materials to explore their response to ion irradiation and recovery mechanisms.

In this work, three Cs-rich hollandite samples with different B-site dopants were selected as model systems for a detailed radiation damage study because of previously reported superior thermodynamic stability and chemical durability [7,8,14]. The hollandite samples were irradiated by 1.1 GeV Au ions to study effects of B-sites dopants on radiation stability. Structural characterization was performed across different length-scales (powder X-ray diffraction, Raman spectroscopy and neutron total scattering) and linked to thermodynamic measurements (high-temperature oxide melt solution calorimetry and differential scanning calorimetry) to gain further insight into radiation damage formation and potential thermal annealing induced recovery in tunnel structured hollandite materials.

2. Experimental methods

$Cs_{1.33}Ga_{1.33}Ti_{6.67}O_{16}$ (CGTO), $Cs_{1.33}Fe_{1.33}Ti_{6.67}O_{16}$ (CFTO), and $Cs_{1.33}Zn_{0.67}Ti_{7.33}O_{16}$ (CZTO) hollandite samples were synthesized by conventional solid-state reaction with experimental details on preparation reported in prior studies [7,8,14]. As-synthesized hollandite samples were further processed by high-energy ion irradiation and thermal annealing resulting in a range of different structural states which were analyzed by complementary techniques. The structural states are defined from here on as follows: (1) As-synthesized samples labelled as "*pristine*", (2) samples exposed to high-energy ion irradiation labelled as "*irradiated*", and (3) irradiated samples processed by thermal annealing at high temperatures labelled as "*annealed*".

Pristine samples were irradiated by 1.1 GeV Au ions at room temperature to a fluence of 5×10^{12} ions/cm^2 using the X0 branch of the UNILAC accelerator of the GSI Helmholtz Center for Heavy Ion Research in Darmstadt, Germany. For irradiation, samples were pressed into aluminum holders with custom milled 1 cm diameter chambers of 50-μm depth. The thickness of each sample inside the chamber was chosen to ensure that the ions completely penetrated the samples and that the energy deposition was relatively uniform (sample thickness: ~30 μm). The sample chambers were then wrapped in 7-μm aluminum foil and exposed to the ion beam; due to the Al-foil, the ion energy upon entering the sample was 930 MeV. The energy loss versus range calculation were performed with the SRIM code [25] assuming a density correction factor for cold, uniaxial compression of powder at small loads: $dE/dx_{CGTO} = 38 \pm 2$ keV/nm, $dE/dx_{CFTO} = 37 \pm 2$ keV/nm, and $dE/dx_{CZTO} = 38 \pm 2$ keV/nm. The uncertainty values represent the upper and lower bounds to the linear energy loss over the sample thickness. Five sample holders per sample type were irradiated, each loaded with 10.8 mg of powder. Additional details concerning this experimental scheme can be found elsewhere [22-24,26].

Neutron total scattering experiments were conducted on the unirradiated and irradiated hollandite samples using the Nanoscale Ordered Materials Diffractometer (NOMAD) at the Spallation Neutron Source (SNS) of Oak Ridge National Laboratory (ORNL) [27]. Between 50 and 100 mg of sample powder was loaded into 2 mm diameter quartz capillaries (0.1 mm wall thickness) and measured at room temperature for 60 min. An identical empty capillary was measured for the same duration and was used for background subtraction. The time-of-flight detectors were calibrated with scattering from diamond and silicon powder. To acquire the scattering structure function, $S(Q)$, the sample scattering intensity was normalized to that from a solid vanadium rod. The pair distribution function, $G(r)$, was obtained through a Fourier transformation of the structure function:

$$G(r) = \frac{\pi}{2} \int_{Q_{min}}^{Q_{max}} Q[S(Q) - 1]\sin(Qr)dQ \quad (2\text{-}1)$$

where r is the radial coordinate. The scattering vector, Q, is defined as:

$$Q = \frac{4\pi \sin\theta}{\lambda} \quad (2\text{-}2)$$

where θ is the neutron scattering angle and λ is the neutron wavelength. Neutron diffraction data was analyzed using Rietveld refinement within the General Structure Analysis System (GSAS) program [28]. Neutron pair distribution functions (PDFs) were analyzed through small box refinement in real space using PDFGui [29] from $r = 1.5$-15.0 Å. The only difference between the refinements of pristine and irradiated samples is that a "spdiameter" parameter was refined for irradiated samples (which were largely amorphous) allowing for the simulation of the material as being an amorphous domain [26]. Analysis of refined crystal structures was performed with VESTA [30].

Complementary structural characterization was performed using powder X-ray diffraction (XRD) and Raman spectroscopy. The XRD data were collected from 10 to 70° 2θ with a 0.02° step size on a Rigaku Ultima IV diffractometer with monochromatic Cu Kα radiation ($\lambda = 1.54$ Å). The intensity of the XRD spectra for each sample was normalized with respect to the strongest peak. Raman spectroscopy was executed with a Horiba LabRAM HR Evolution Raman microscope using a 532 nm laser with 5 mW output power.

High-temperature oxide melt solution calorimetry was performed using an AlexSYS 1000 calorimeter (SETARAM) operat-

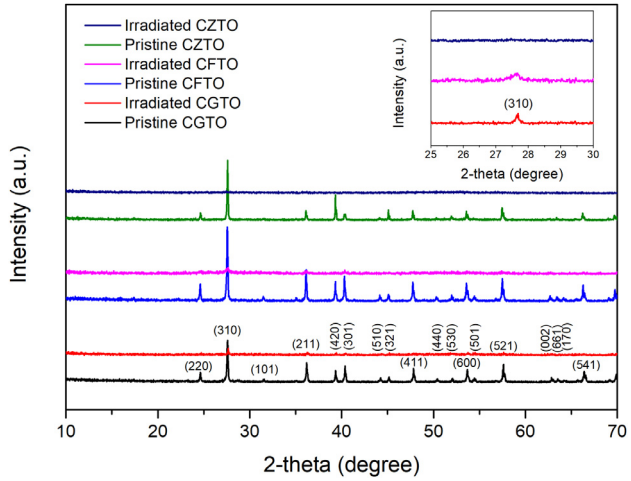

Fig. 1. XRD patterns of CGTO, CFTO, and CZTO hollandite before (pristine) and after (irradiated) ion-beam exposure to 1.1 GeV Au ions to a fluence of 5×10^{12} ions/cm^2. The major Bragg maxima of the tetragonal hollandite structure are indexed for the pristine CGTO sample. The inset shows partial XRD patterns of corresponding irradiated hollandite in Fig. 1.

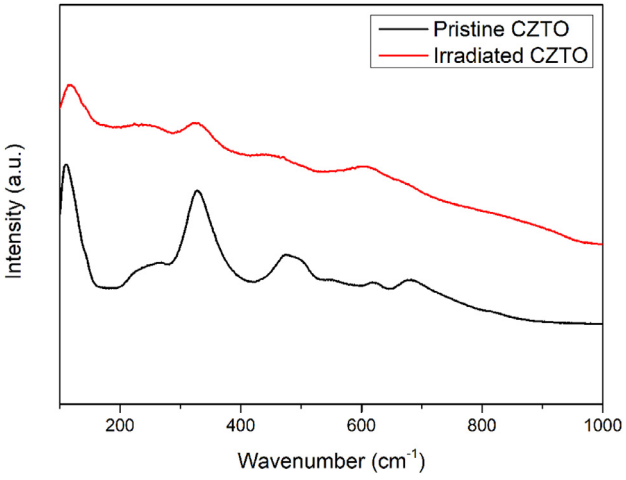

Fig. 2. Raman spectra of pristine and irradiated CZTO hollandite.

Table 1
Wavenumbers (cm^{-1}) of observed Raman peaks and mode assignment of pristine and irradiated CZTO hollandite.

Wavenumber (cm^{-1})		Mode assignment
Pristine sample	Irradiated sample	
110	114	E_g
190-290	200-280	A_g, B_g
328	324	A_g
475	-	E_g
618	605	B_g
683	-	B_g

ing at 702°C. In a drop solution calorimetry experiment, ~1-5 mg weighed powder sample was loosely pressed into a pellet and dropped from room temperature into the molten sodium molybdate ($3Na_2O{\bullet}4MoO_3$) solvent in a platinum crucible in the calorimeter. The calorimeter assembly was flushed with air at ~50 mL/min. Moreover, air was bubbled through the solvent at ~5 mL/min to stir the melt and improve sample dissolution. The calorimeter was calibrated using the heat content of high purity α-alumina (Alfa Aesar, 99.997%). Detailed instrument and experimental procedures have been well established and described by Navrotsky [31,32]. The difference of enthalpies of drop solution between pristine and irradiated samples directly gives the enthalpy of damage at room temperature.

Differential scanning calorimetry (DSC) was performed on a NETZSCH STA 449 F3 Juptier instrument. Ar gas with 20 mL/min flow rate was used to provide an inert atmosphere. The sensitivity of the DSC instrument was calibrated on the basis of an alumina heat capacity curve. Several runs using an empty crucible under the same condition were performed before the sample runs to ensure reproducibility of the baselines. Approximately 1-2 mg of the irradiated CGTO and CFTO samples was loaded in an alumina crucible for DSC measurements as there was no remaining irradiated CZTO sample after solution calorimetry. The samples were heated to 1200°C at 10°C/min, followed by isothermal holding at 1200°C for 5 min and subsequent cooling to room temperature at 20°C/min. A second DSC run under the same condition was conducted without disturbing the furnace to maintain the geometry of the samples. The DSC curve of the second run was used to correct the baseline since no appreciable thermal effect was found [24,33].

3. Results

3.1. Radiation-damage formation

Fig. 1 displays XRD patterns of pristine and irradiated CGTO, CFTO, and CZTO. For all pristine samples, the observed XRD peaks can be assigned to a well-crystallized tetragonal hollandite structure ($I4/m$) regardless of the B-sites dopant identity. Negligible peak shifts of the (310) plane indicated that no significant changes of the unit cell were caused by B-site dopants. After ion irradiation, diffusive background scattering was exhibited for all irradiated samples, indicative of a reduction in intensity of the diffraction maxima due to ion beam-induced amorphization. Nevertheless, the level of amorphization was distinct for each sample composition (the inset of Fig. 1). For example, irradiated CZTO was almost fully amorphized because its XRD pattern did not show clear Bragg peaks indicative of long-range order. Remnant diffraction maxima of both irradiated CGTO and CFTO, indicated that a small amount of crystallinity was present after ion irradiation.

Fig. 2 displays the Raman spectra of pristine and irradiated CZTO hollandite. The assignment of the different Raman modes is summarized in Table 1. For the pristine sample, five relatively sharp peaks are observed at ~110, ~328, ~475, ~618, and ~683 cm^{-1}, while a broader feature is apparent between 200 and 280 cm^{-1}. The peaks at ~110 and ~475 cm^{-1} may be attributed to the symmetric stretching modes of $(B,Ti)O_6$ octahedra, while the peaks at ~328, ~618, and ~683 cm^{-1} along with the broad feature between 200 and 280 cm^{-1} may result from the bending modes of $(B,Ti)O_6$ octahedra [14,34-40]. Compared with the pristine sample, the intensity of all Raman peaks in the irradiated sample were significantly diminished, although the shape and peak position were maintained for the most intense modes (Fig. 2). The peaks with lower intensity in the pristine sample (e.g., the peaks at ~475 and 683 cm^{-1}) were indistinguishable from the background signal after ion irradiation. The changes in the peak intensities after ion irradiation suggest that the short-range structure related to the $(B,Ti)O_6$ octahedra was altered by the energy deposition from the ion beam.

Fig. 3 shows neutron total scattering structure functions, $S(Q)$, of all three pristine and irradiated hollandite samples. Rietveld refinement of pristine samples reveals that a small amount of unreacted TiO_2 rutile was present in each sample and this impurity phase is most evident as a small shoulder at ~2.85 Å^{-1} in pristine CZTO (Fig. 3c). The unit cell parameters and the weight fraction of TiO_2 rutile for each tetragonal hollandite sample is summarized in Table 2. The varying amount of TiO_2 rutile is common for the

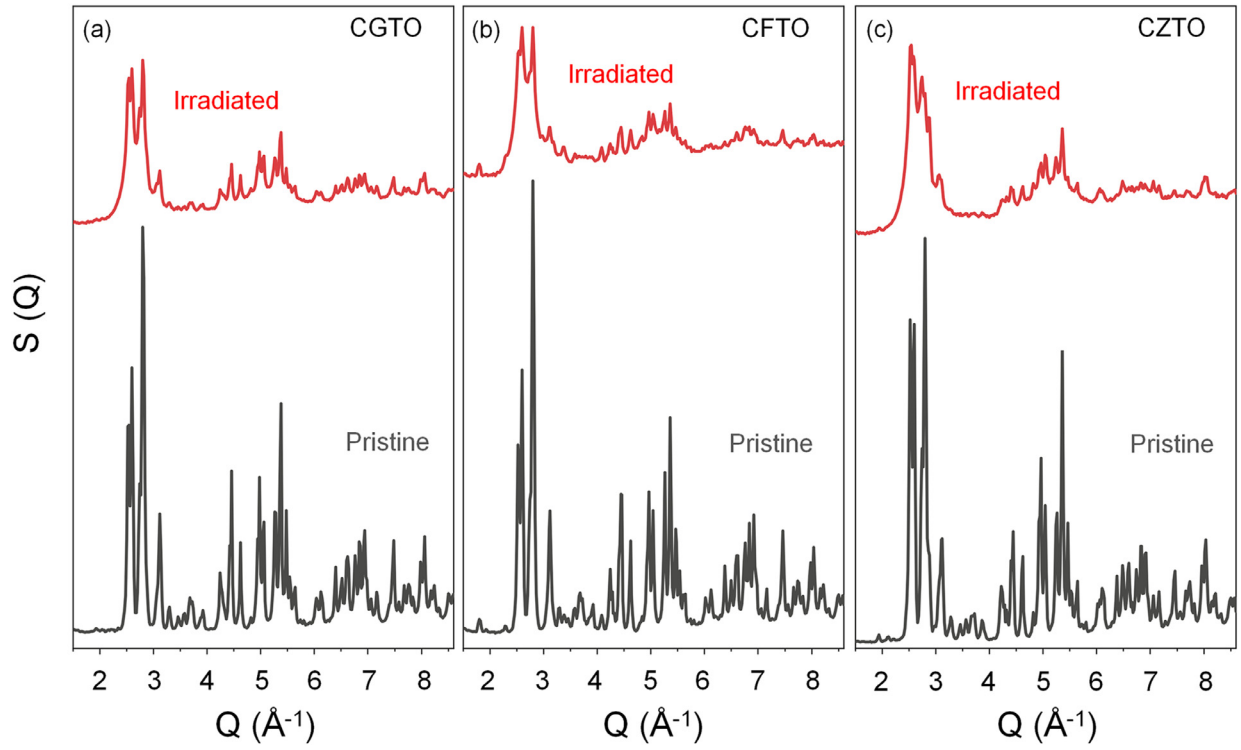

Fig. 3. Neutron total scattering structure functions of (dark grey) pristine and (red) irradiated (a) CGTO, (b) CFTO, and (c) CZTO.

Table 2
Rietveld refinement results of neutron diffraction data of pristine samples.

Composition	a = b (Å)	c (Å)	TiO_2 rutile (wt.%)	R_{wp} (%)
CGTO	10.2513(6)	2.9586(2)	5(1)	6.4%
CFTO	10.2663(7)	2.9646(3)	2(1)	6.2%
CZTO	10.2769(7)	2.9681(3)	12(1)	7.8%

hollandite-type materials and the quantity of this impurity phase depends on the ionic radii of the B-site dopants. Typically, larger difference of ionic radius between the Ti^{4+} and the B-site dopants would result in more TiO_2 rutile [41]. In addition, the amount of TiO_2 rutile in Table 2 was used to correct the enthalpy data obtained from high-temperature oxide melt solution calorimetry. After ion irradiation, the structure functions are modified but maintain qualitatively similar features: diminished Bragg peak intensity and increased background scattering. The broad oscillatory diffuse scattering, most pronounced as bands from ~2-3 $Å^{-1}$ and ~4-5.5 $Å^{-1}$, is indicative of amorphization. The TiO_2 rutile phase is largely unaffected by ion irradiation and the shoulder at ~2.85 $Å^{-1}$ in pristine CZTO becomes a distinct low-intensity peak in irradiated CZTO due to the decrease in intensity of the hollandite diffraction maxima.

The long-range structural data agree for XRD (Fig. 1) and neutron diffraction and show that the propensity of amorphization increases from CZTO to CFTO and to CGTO. Fourier transformation of the neutron structure functions yields the pair distribution functions (PDFs) which provide further insight into the atomic-scale changes induced by the swift heavy ions (Fig. 4). The PDFs of all pristine samples up to a *r*-space of $r_{max} = 15$ Å were well-modeled ($R_{wp} < 9.6\%$) with a phase mixture of hollandite and TiO_2 rutile. The difference curves show that the tetragonal structural model displayed a subtle mismatch with the experimental data at ~2 Å in pristine CFTO and CZTO which can be explained by structural relaxations associated with variations of ionic radius between the B-site dopants (i.e., $Fe^{3+} = 0.645$ Å and $Zn^{2+} = 0.74$ Å) and Ti^{4+}

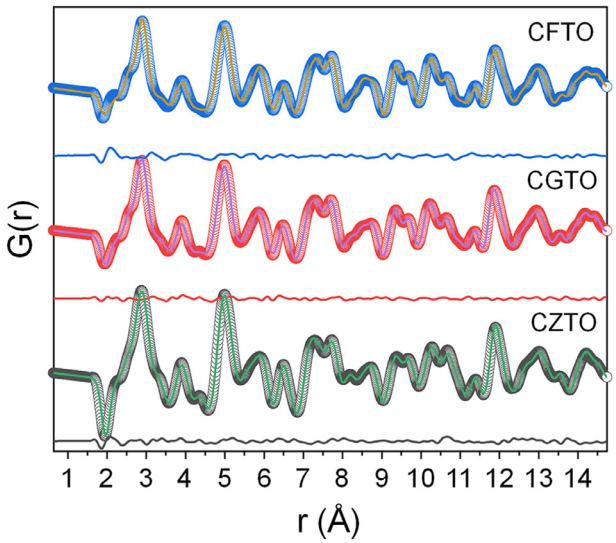

Fig. 4. Neutron PDFs of pristine CFTO, CGTO, and CZTO hollandite with small box refinement using a tetragonal (I4/m) structural model. The difference curves below the PDF show the difference between model and experimental data.

(0.605 Å) [42]. This is supported by the fact that the model fit is much better for CGTO in which the ionic radius of Ga^{3+} (0.62 Å) is close to that of Ti^{4+} [42]. A similar phenomenon has been previously reported in disordered spinel oxides also investigated by total neutron scattering [43]. Despite the subtle local deviation of CFTO and CZTO from the ideal hollandite structure, the short-range data do not show any other noticeable deviations from the ideal *I*4/*m* hollandite structural model.

The small box refinement of PDFs yields additional structural information at atomistic length-scale (Table 3). Besides various atomic correlations, the structural refinements of the PDFs corre-

Table 3
Structural information obtained from small box refinement of neutron PDFs from pristine and irradiated hollandite samples. Baur's Distortion index (DI, Eq. (3-1)) for each polyhedron is given; the standard deviation from the average of the 3 nearest-neighbor B-B distances are reported as σ. The percentage changes of the PDFs before (pristine) and after (irradiated) ion irradiation is given as well.

Pristine							
Composition	Average <B-O> bond length (Å) / DI	Average <Cs-O> bond length (Å) / DI	Average <B-B> distance of 3 N.N. distances (Å) / σ				
CGTO	1.97 / 0.010	3.08 / 0.049	3.20 / 0.289				
CFTO	1.98 / 0.025	3.09 / 0.051	3.19 / 0.359				
CZTO	1.98 / 0.011	3.11 / 0.051	3.21 / 0.291				
Irradiated							
Composition	Average <B-O> bond length (Å) / DI	Average <Cs-O> bond length (Å) / DI	Average <B-B> distance of 3 N.N. distances (Å) / σ				
CGTO	2.00 / 0.033	3.07 / 0.043	3.23 / 0.198				
CFTO	2.02 / 0.081	3.15 / 0.086	3.26 / 0.463				
CZTO	2.05 / 0.078	3.04 / 0.162	3.24 / 0.213				
Change							
Composition	Average <B-O>	DI of average <B-O>	Average <Cs-O>	DI of average <Cs-O>	Average <B-B>	σ of average <B-B>	
CGTO	1.2%	229.0%	-0.2%	-12.3%	1.1%	-31.7%	
CFTO	1.9%	224.9%	2.2%	69.5%	2.3%	29.1%	
CZTO	3.6%	628.5%	-2.2%	219.2%	0.9%	-27.0%	

sponding to the irradiated samples yielded the Baur's distortion indices (DI) [44] of the cation-anion coordination polyhedra (Table 3) defined as:

$$DI = \frac{1}{n}\sum_{i=1}^{n}\frac{|l_i - l_{av}|}{l_{av}} \tag{3-1}$$

where n is the number of cation-anion bonds, l_{av} is the average bond length of the coordination polyhedra, and l_i is the bond length of the i^{th} cation-anion bond. The DI describes the displacement of the cation away from the ideal geometric center of its coordination polyhedron (a coordination polyhedra with all equidistant cation-anion lengths has a DI of 0). Despite different B-site dopants in each hollandite composition, the local environment of the Cs ions within the tunnels was not noticeably impacted as evidenced by the negligible difference in average <Cs-O> bond length and the DI values among all three pristine samples.

However, the bonding environment of the B-O framework changed significantly with different B-site dopants. Although the average <B-O> bond length was very similar in all samples, in an excellent agreement with Pauling's 1st rule [45] (the cation-anion bond length is the sum of the cationic and anionic radii), the corresponding B-O framework was distorted to a different degree with the various B-site cations. This behavior was largely attributed to the Zachariasen effect [46,47], which states that imbalances in cation-anion bond strengths created by aliovalent doping can be largely removed by lengthening some cation-anion bonds and shortening others. For example, CFTO with one short and one long polar oxygen bond had the largest displacement along the polar axis, which is reflected in the largest DI value among all three chemical compositions. The B-O framework can also be described through the three nearest neighbor (3 N.N.) distances of the B-site cations as shown in Fig. 5. The B-site cation (large blue circle) in each sample has two short B-B distances (large blue circle – green circle & large blue circle – red circle) and one long B-B distance (large blue circle – brown circle); the standard deviation (σ) of the three distances describes how far the adjacent (100) planes are from forming ideal triangular nets of B-site cations. The spread of these three distances is largest among the three samples for pristine CFTO and is largely attributable to the B-site cations (Fe and Ti) residing the farthest from the geometric center of their coordination polyhedra (Table 3).

The irradiation-induced changes to the local structure for the different hollandite compositions are evident by comparing the PDFs of the irradiated (red curves) with the pristine, reference (gray curves) samples (Fig. 6). Detailed structural analysis of the PDFs was performed *via* small-box modeling (Table 3). Amorphization is evident in each sample as a decrease of peak area in the region beyond the coordination polyhedra ($r > \sim$4 Å). However, the very local radiation response at the level of the coordination polyhedra shows a distinct dependence on the B-site dopant: (*i*) The average <B-O> bond length of CGTO (Fig. 6b) is increased after irradiation; the distortion in the $(Ga,Ti)O_6$ octahedra was larger along the polar axis, while the distortion along the equatorial axis remains mostly unchanged. For the O-O correlation peak (r = 2.5-2.9 Å), the r-position of the peak maximum was largely unchanged after irradiation. (*ii*) The average <B-O> bond length increased in irradiated CFTO (Fig. 6c) with larger distortions in the $(Fe,Ti)O_6$ octahedra but in this case along the equatorial axis rather than the polar axis. There is one short and one long B-Cs distance in CFTO due to symmetry and the irradiation-induced distortion along the equatorial axis further reduces the short distance and enlarges the long distance. This is evident in Fig. 6c as the B-Cs correlation peak at $r = \sim$3.8 Å merges into the background after irradiation. The B-O correlation peak at $r = \sim$1.95 Å in pristine CFTO splits after irradiation into two low-intensity peaks (r = 1.8-2.2 Å) with distinct peak

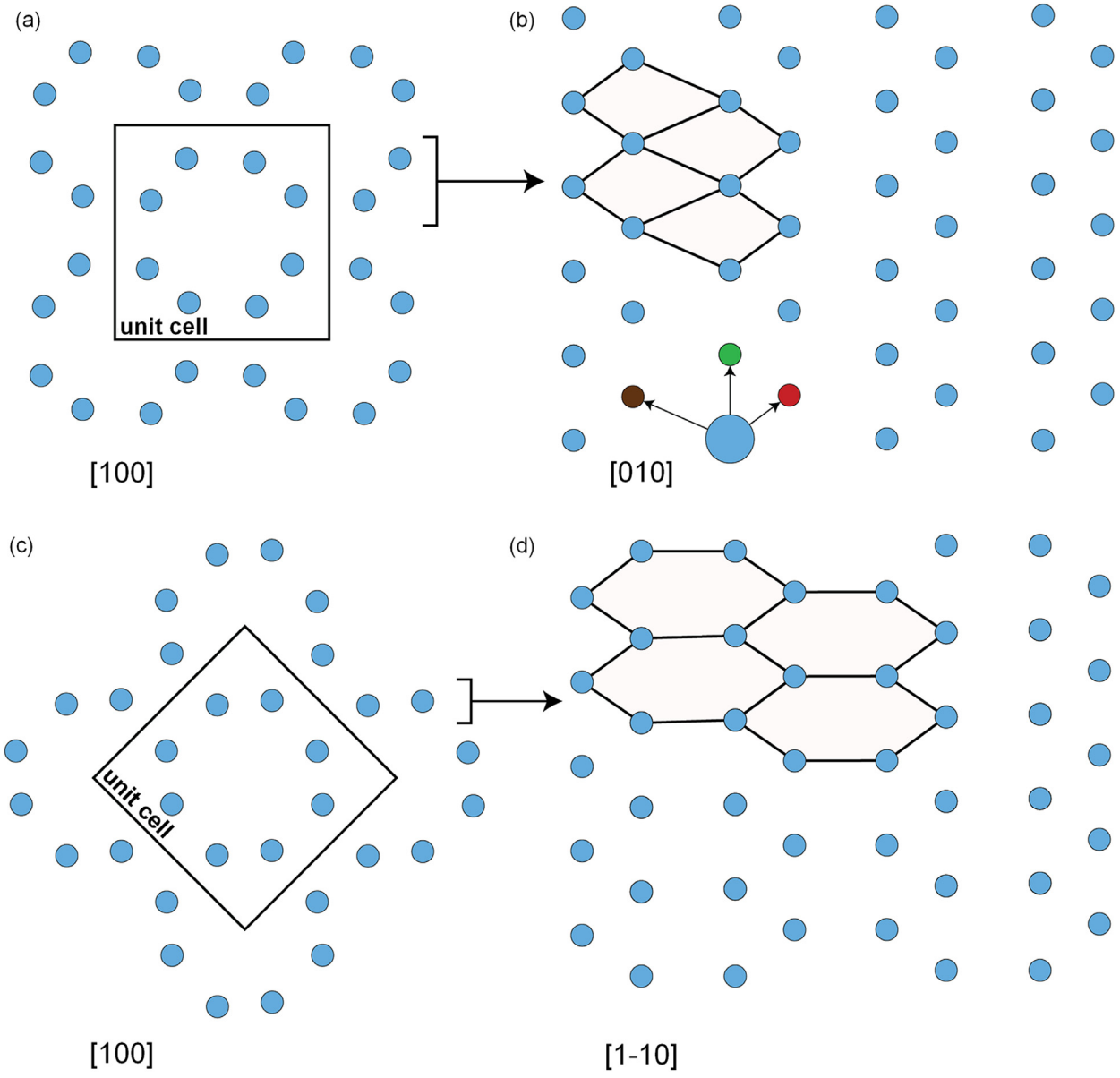

Fig. 5. The B-site cation (blue circles) network in the hollandite structure. When viewing down the [100] direction (a & c), the B-site cation network can be imagined as forming different layered arrangements: an elongated triangular net in the [010] direction (b) and an elongated honeycomb lattice in the [1-10] direction (d). The 3 N.N. <B-B> distances in adjacent (100) planes are emphasized in (b).

shifts away from the preirradiated peak position which suggests a reduction of Fe/Ti coordination number.

In contrast to CGTO, the behavior of the oxygen sublattice in CFTO shows a larger rearrangement of the local structure as evident by the growing O-O correlation at $r = \sim 2.6$ Å. (*iii*) The peak shift at $r = 1.98$ Å to lower *r*-values indicates that the average <B-O> bond length of CZTO (Fig. 6d) decreased after irradiation; however, small-box refinement shows that the average <B-O> bond lengths are actually increasing concomitant with a distinct distortion in the $(Zn,Ti)O_6$ octahedra (Table 3). The shift of the negative peak to lower-*r* and the changes in the feature at $r = 2.4$-2.5 Å after irradiation can be explained by the i-values of five out of the six B-O bond lengths being in the region $r = 1.83$-2.1 Å, while the sixth bond length is at $r = \sim 2.43$ Å. This behavior can be attributed to an irradiation-induced reduction of the Zn/Ti coordination number as Zn prefers fourfold coordination in the ZnO wurtzite structure. In terms of directionality, the large distortion in the $(Zn,Ti)O_6$ octahedra occurs along both the polar and equatorial axes. The intensity of the O-O correlation peak is slightly decreased after ion irradiation. Small box refinement of the PDFs collected from the irradiated samples reveals that the structural response of the Cs-O and B-B bonds to ion irradiation is distinctly different for each sample composition. Using the hollandite model corresponding to the pristine samples as a starting point, all fits to the PDFs collected from the irradiated samples were obtained with goodness-of-fit parameters of $R_{wp} < 21$ %; the increase in R_{wp}, relative to the refinements of the PDFs of the pristine samples, is predominately due to the structural refinement of a largely amorphous material using a model corresponding to a crystalline phase [26] because of the lack of ability to model how these different amorphous "units" or "building blocks" are arranged with respect to one another. Regardless, this approach is useful in probing fundamental pair correlations within the amorphous phase [26]. The average <Cs-O> bond distance remains nearly unchanged in CGTO, but the Cs ions move closer to the center of the coordination cube after irradiation as shown by the smaller DI values (Table 3). This is in clear con-

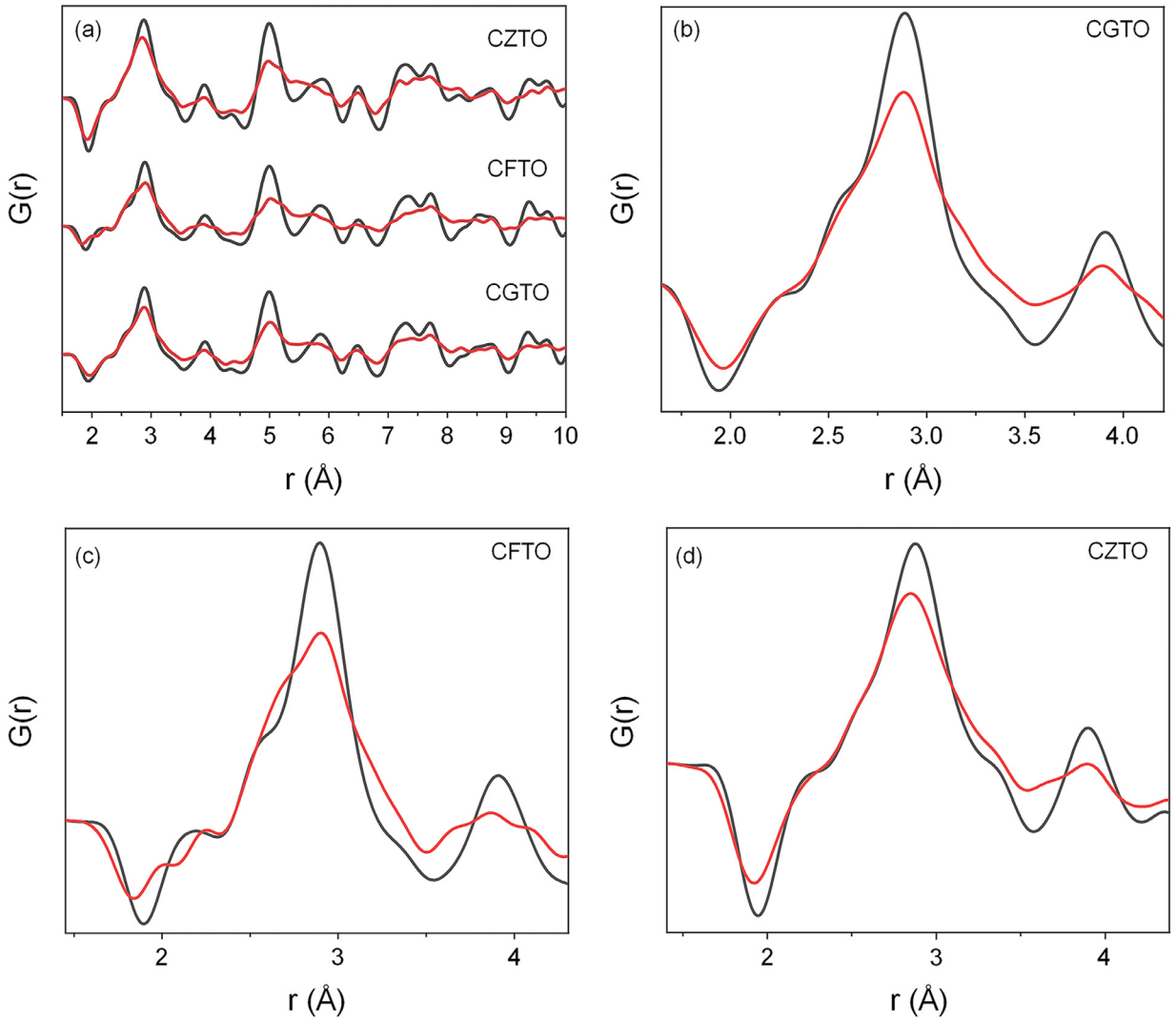

Fig. 6. (a) Neutron PDFs of all three hollandite samples before (grey) and after (red) ion irradiation with 1.1 GeV Au ions. The PDFs corresponding to the local bonding polyhedra of the pristine (grey) and irradiated (red) samples are shown for (b) CGTO, (c) CFTO, and (d) CZTO.

trast to CFTO and CZTO, for which the Cs ions move farther away from the center position of the coordination cube (Table 3). Interestingly, the Cs ions move within the tunnels in irradiated CFTO with an elongated average <Cs-O> bond length to maintain the Cs ions "captured" in cubic coordination.

The Cs movement within the tunnels is observed in CZTO, but the average <Cs-O> bond length is decreased forcing the Cs ions toward a face of the coordination cubes. This process disrupts the local bonding environment of the Cs-O network in CZTO, which explains the significant distortion of the $(Zn,Ti)O_6$ octahedra described above. The spread of the <B-B> bond distances becomes smaller after ion irradiation for CGTO and CZTO suggesting that the nearest neighbor planes of B-site cations are more regular in the irradiation-induced structure. In contrast, the spread of the <B-B> bond distances in CFTO increases after ion irradiation due to a shortening and elongation of distances between edge-sharing B-site cations and corner-sharing B-site cations, respectively.

High-temperature oxide melt solution calorimetry was performed on pristine and irradiated samples to obtain enthalpies of drop solution ΔH_{ds} (Table 4 & Fig. 7a), which were used to compare the energy landscape between different states (i.e., pristine *versus* damaged). It is notable that the amount of TiO_2 rutile in Table 2 was used to correct ΔH_{ds}. The methodology to correct the ΔH_{ds} for the hollandite sample with minor amount of secondary phase (TiO_2 rutile) has been used in a prior study [41]. The enthalpic difference in ΔH_{ds} between the pristine and irradiated samples represents the enthalpy of damage (ΔH_{dmg}), which can be used as a measure of radiation stability for each composition. Smaller values of ΔH_{dmg} indicate enhanced stability to energetic heavy ion irradiation with smaller levels of radiation damage. The pristine samples are largely endothermic with values of ΔH_{ds} on the order of 450 kJ/mol. The corresponding ΔH_{ds} of the irradiated samples are significantly decreased with some compositions changing from an endothermic to an exothermic behavior. Irradiated CGTO remains endothermic, whereas the enthalpies of drop solution of irradiated CFTO and CZTO becomes exothermic (Table 4).

The large average enthalpies of damage ΔH_{dmg} (Fig. 7b) show that ion irradiation can significantly destabilize the well-crystallized hollandite samples by beam-induced transformations into an amorphous state with destruction of the characteristic tunnel structure. Among all three samples, the value of ΔH_{dmg} is the largest for CZTO (1203.5 ± 117.6 kJ/mol), while CGTO has the smallest value (378.0 ± 3.4 kJ/mol). The relatively large errors of ΔH_{dmg} can be explained by the limited amount of irradiated sample mass available for calorimetric experiments. A comparison

Table 4
Enthalpies of drop solution (ΔH_{ds}) of pristine and irradiated samples in $3Na_2O{\cdot}4MoO_3$ at 702°C with two standard errors.

Sample	Mass (mg)	ΔH_{ds} (kJ/mol)[a]	ΔH_{dmg} (kJ/mol)[a]
Pristine CGTO	~5	471.2 ± 3.3 (6)	N/A
Irradiated CGTO_1	3.28	94.3	N/A
Irradiated CGTO_2	2.31	92.2	N/A
Irradiated CGTO (average)	N/A[b]	93.3 ± 1.0 (2)	378.0 ± 3.4 (2)
Pristine CFTO	~5	481.6 ± 7.9 (6)	N/A
Irradiated CFTO_1	1.55	-225.2	N/A
Irradiated CFTO_2	1.13	-544.9	N/A
Irradiated CFTO (average)	N/A	-385.1 ± 159.8 (2)	866.7 ± 160.0 (2)
Pristine CZTO	~5	417.6 ± 6.3 (6)	N/A
Irradiated CZTO_1	2.98	-903.5	N/A
Irradiated CZTO_2	2.50	-668.5	N/A
Irradiated CZTO (average)	N/A	-786.0 ± 117.5 (2)	1203.5 ± 117.6 (2)

[a] **Value is the mean of the number of experiments indicated in the parentheses. Error is the two standard deviations of the mean.** [b] **N/A is not applicable.**

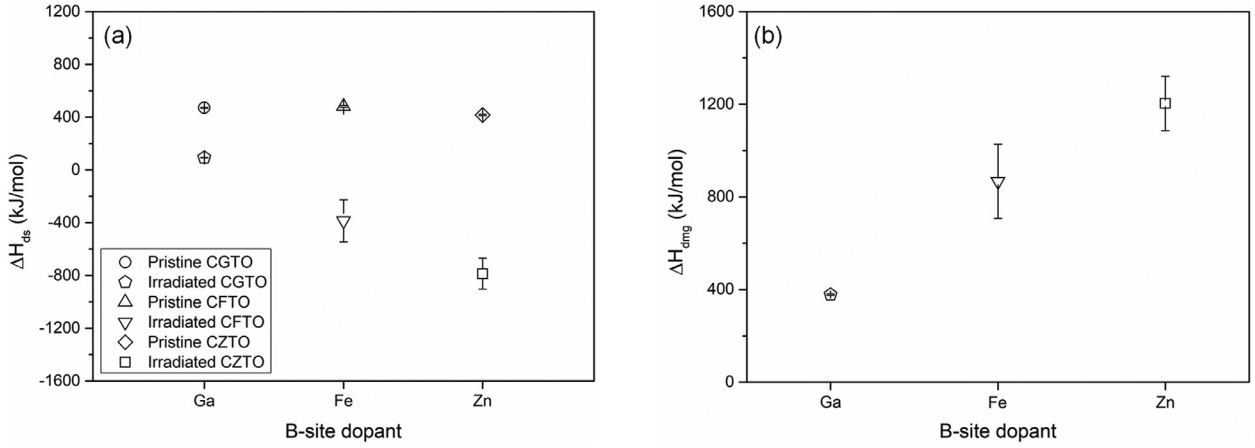

Fig. 7. (a) Enthalpies of drop solution (ΔH_{ds}) for pristine and irradiated CGTO, CFTO, and CZTO, (b) average enthalpies of damage (ΔH_{dmg}), determined by the difference in ΔH_{ds} between the pristine and irradiated samples, for the CGTO, CFTO, and CZTO.

of ΔH_{dmg} among all three samples reveals that CGTO hollandite has the best radiation stability. This agrees to a prior study with intermediate-energy ions (<1 MeV) of predominantly nuclear energy loss which showed that CGTO has a larger radiation-damage tolerance than CZTO [17].

3.2. Thermal annealing induced recovery

Irradiated CGTO and CFTO were annealed at 1200°C for 5 min and subsequently cooled down to room temperature. Two cycles were performed for each sample. It is notable that there is not remaining irradiated CZTO available for thermal annealing. XRD and Raman spectroscopy were used to investigate the structural changes before and after annealing over the long-range and short-range, respectively. XRD patterns of the CFTO (Fig. 8a) show that the diffraction maximum of the (310) plane was strongly reduced in the irradiated sample in agreement with ion-induced amorphization. The same behavior was also observed for the CGTO (patterns not shown). The XRD patterns show no significant changes after annealing up to 1200°C indicating that this heat treatment was insufficient to restore the long-range structure. In contrast, pristine and annealed CFTO share the major bands and the intensity and width for their two strongest bands is similar (Fig. 8b), suggesting that the vibrational modes are attributed to the BO_6 octahedra framework. A few relatively weak bands (labeled as "*" in Fig. 8b) were found in annealed CFTO, indicating the formation of new structures in the local environment other than the BO_6 octahedral framework. The emerging vibrations resulted from the new local rearrangement between the B-site dopants (e.g., Fe or Ti) with less coordination to the neighboring oxygen lattice. It is also likely that these emerging vibrations can be attributed to the formation of defect clusters of Ti^{3+} and O_2^- [48]. According to a prior study [48], thermal treatment may create a new local environment resulting from previous irradiation-induced defects. The development of the oxygen-related defects may be due to the severely damaged structure and Ar atmosphere. Other possibilities leading to new vibrations have been considered as well, such as the formation of α-Fe_2O_3 and TiO_2 rutile, and the background signal from the glass substrates [37,49,50]. However, the Raman peaks could not be matched to these primary phases. In addition, none of these phases was detected in post-annealing XRD studies. A more comprehensive investigation of the newly formed local vibrations will be a topic of future work.

Fig. 9 shows the DSC profiles of irradiated CGTO and CFTO. For both samples, two exothermic events were observed as evidenced by two distinct peaks in different temperature regions. The two peaks were located at similar temperature regions for both samples. The first peak starts from ~200°C and ends at ~500°C, while the second peak occurs between ~500°C and ~800°C. Due to the annealing within an inert Ar atmosphere it is unlikely that the exothermic events were caused by chemical reactions and they can be attributed to structural changes induced by thermal annealing. Two exothermic peaks suggest that the structural changes were completed in two separate processes at different temperatures. No appreciable peaks appeared in the second run indicating that structural changes were completed after the first run. The total heat release associated with the exothermic reactions is 7.7 J/mg (i.e., −6525 kJ/mol) and 4.6 J/mg (i.e., −3842 kJ/mol) for CGTO

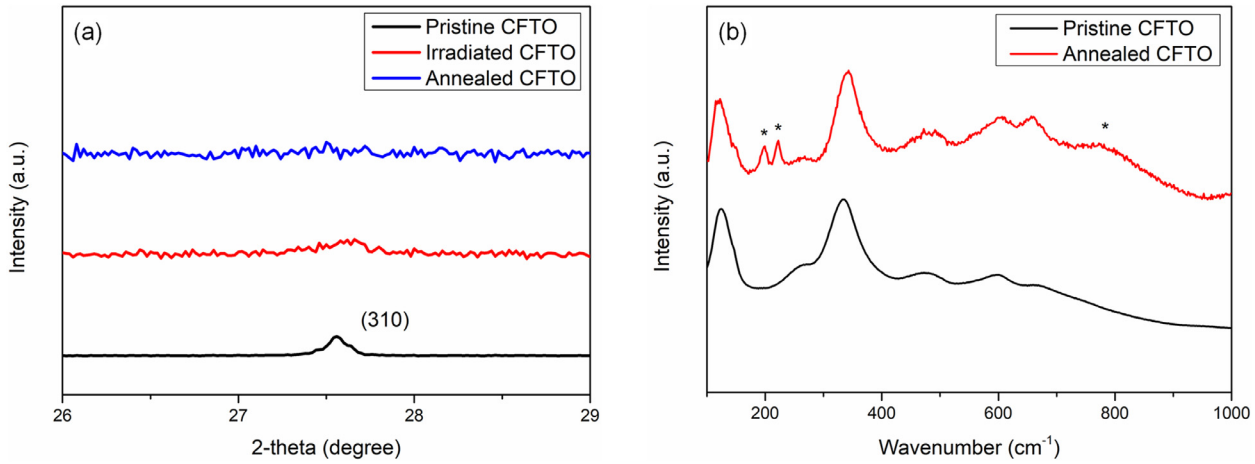

Fig. 8. (a) XRD patterns of pristine, irradiated, and annealed CFTO, (b) Raman spectra of pristine and annealed CFTO. "*" represents vibrations from formation of new structure in the local environment other than BO_6 octahedra framework.

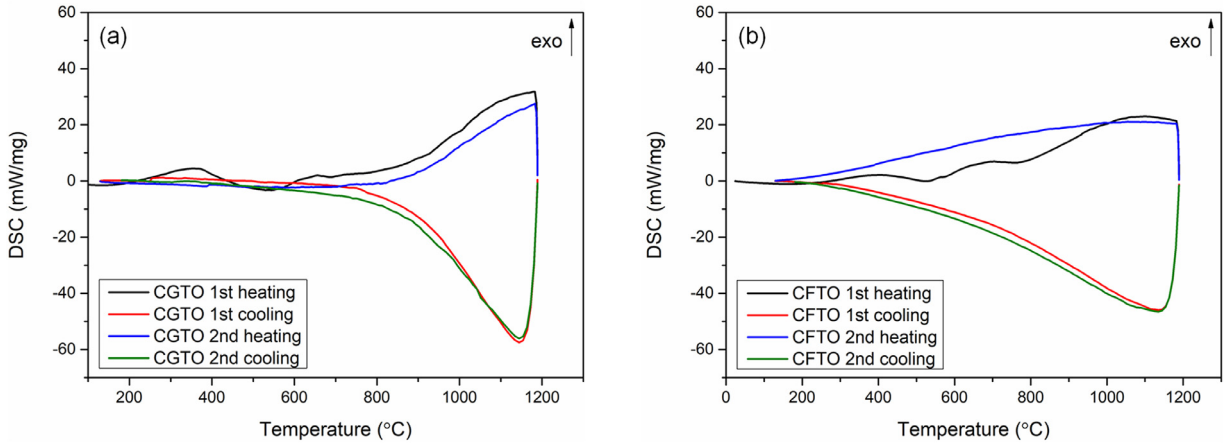

Fig. 9. The DSC profiles of (a) irradiated CGTO and (b) irradiated CFTO.

and CFTO, respectively. The total heat release was calculated based on the molecular weight of the corresponding pristine analogues. The total heat release for the two samples was sufficient to compensate their ΔH_{dmg} induced by high-energy ion irradiation which indicates completion of potential structural changes in irradiated hollandite after thermal annealing under these conditions.

4. Discussion

Neutron PDF analysis indicates a quite different local radiation responses of the three hollandite samples with different B-site dopants. This is in contrast to the behaviors observed in diffraction data over length-scales which show a similar crystalline-to-amorphous transformation. However, the rate of amorphization is also different among the three samples. The detailed radiation response of the hollandite structure under swift heavy ion irradiation was determined by the identity of the B-site dopant. In the case of CFTO, the local structure was modified in a way that constrains the Cs ions within a cubic coordination at the expense of the symmetry of the $(B,Ti)O_6$ octahedra and the B-B sublattice framework. This is different to CZTO, for which the local atomic arrangement prioritizes to maintain the symmetry of the B-B sublattice at the expense of the symmetry of the $(B,Ti)O_6$ octahedra as well as the coordination environment of the Cs ions. Intriguingly, CGTO preserves the integrity of the hollandite tunnel structure over the short-range with some relaxation of the B-site cations along the polar axes of the $(B,Ti)O_6$ octahedra while maintaining the cubic coordination of the Cs ions.

It may be more instructive to consider the simple binary oxide forms for each B-site dopant to analyze the radiation response, because the local environment around the dopant resembles most closely the corresponding environment that the cation adopts in the binary oxide form. The structure of ZnO is wurtzite ($Cs_{1.33}Zn_{0.67}Ti_{7.33}O_{16}$) which consists of layers of ideal triangular nets of Zn cations in between triangular nets of oxygen. The structure of Fe_2O_3 is corundum ($Cs_{1.33}Fe_{1.33}Ti_{6.67}O_{16}$) which consists of 2/3 dense triangular nets forming an ideal honeycomb structure in between triangular nets of oxygen [51]. Interestingly, monoclinic β-Ga_2O_3 ($Cs_{1.33}Ga_{1.33}Ti_{6.67}O_{16}$) also features layers of triangular nets of oxygen, but the Ga cation fills both octahedral and tetrahedral interstices which create intermediate layers that have features of dense triangular nets and of honeycomb-lattices. The local environment around the B-site dopant may trend towards the layering type of its binary oxide form under ion irradiation. The hollandite structural features a B-site cation layer (100), which is an elongated triangular net, and another layer (1-10) which is an elongated honeycomb lattice (Fig. 5). Among the three cations, Ga is chemically best suited to maintain both layering schemes at the atomic scale because it is also the local environment in the binary oxide form, dictated by its ionic radius and valence. This behavior results in an increased radiation stability, which is supported by the results of solution calorimetry (Fig. 7). The superior radiation

stability of CGTO than that of CZTO has also been observed under lower energy (<1 MeV) ion irradiation [17]. This is the first time for tunnel structured complex oxides that the correlation between radiation stability and the structural features of the constituent binary oxide of the B-site dopant has been established.

The energetics results of the DSC experiments provide more insights associated with the thermal annealing induced structural evolution (Fig. 9). Changes in the local structure of radiation damaged samples after thermal annealing has been observed in pyrochlore systems [24,52-55]. In the present work, the thermal-induced structural evolution occurred in two separate processes in different temperature regions due to two exothermic peaks. Based on the neutron total scattering analysis of the as-irradiated samples, a two-step structural change can be used to explain the thermodynamic results: (1) a rearrangement of the B-site dopant in framework at lower temperatures (~200-500°C) and (2) restoration of the Cs coordination polyhedra at higher temperatures (~500-800°C). In the first process, displaced B-site dopants would move back to their initial position in the BO_6 octahedra framework of the pristine samples over the short-range. It is also likely that some B-site dopants (e.g., the Fe dopants whose coordination number was reduced *via* ion irradiation) resulted in new local vibrational states with neighboring oxygen in the framework. This is supported by the emergence of additional Raman peaks after annealing. The restoration of the Cs-ion polyhedral network occurred in the second process, because Cs ions are more difficult to be displaced at relatively low temperatures compared to B-site dopants.

Structural changes over short-range were induced by thermal annealing, but recrystallization over long-range was not detected after heating up to 1200°C. The annealing-induced structural recovery of the radiation damaged hollandite structure is intricate and this is similar to the decoupled, multi-recovery processes at different length-scales observed in other nuclear related materials. For example, long-range ordering was incomplete after thermal annealing of the Ni-Cr model alloy and the alloy 690 (Ni-30Cr-10Fe) to temperatures at which the short-range structure was recovered [56,57]. The behavior of hollandite is different to the results reported for irradiated $Dy_2Ti_2O_7$ pyrochlore [24] with recovery of the long-range structure before the annealing of the local atomic arrangement at 1200°C.

This difference can be explained based on the energetics and crystallography of the hollandite structure. In pyrochlore, there exists a metastable state (i.e., disordered, crystalline pyrochlore) that is thermodynamically and structurally between the most stable state (i.e., fully ordered, crystalline pyrochlore) and the least stable state (i.e., amorphous pyrochlore), which provides possibly a faster pathway for irradiated pyrochlore to recover the long-range structure to the disordered state *via* thermal annealing [24]. In contrast, the complexity associated with the tunnel structure in hollandite reduces the likelihood that a metastable state exists between the pristine and irradiated phases. The enthalpy of damage, ΔH_{dmg}, for hollandite is ~2-5 times as large as for titanate pyrochlore irradiated under similar conditions [24]. Despite annealing under similar conditions (1200°C for 5 min), the higher enthalpy of damage for hollandite indicates a more severely damaged state that requires higher annealing temperatures for long-range recovery.

5. Conclusions

In this work, three hollandite compositions were synthesized and thereafter irradiated by 1.1 GeV Au ion beam. XRD data showed that there was a crystalline-to-amorphous transformation for all samples, however the rate of amorphization was quite different. Neutron PDF analysis along with Raman spectroscopy indicated that the structure over short-range distances was also altered for each composition. The energy landscape before and after ion irradiation was determined by high-temperature oxide melt solution calorimetry. The Ga-substituted hollandite exhibited the smallest enthalpy of damage indicating the best radiation stability among the three samples. The different radiation response was related to structure and thermochemistry and ultimately was attributed to the structural features of the binary oxide form of the B-site dopants. Structural changes *via* thermal annealing up to 1200°C was further studied for as-irradiated samples. Results of thermal analysis and structural characterization suggested that the thermal annealing-induced structural evolution of the radiation damaged hollandite structure is complicated and decoupled at different length-scales.

Declaration of Competing Interest

The authors declare that they have no known competing financial interests or personal relationships that could have appeared to influence the work reported in this paper.

Acknowledgements

This work was supported by the Center for Hierarchical Waste Form Materials (CHWM), an Energy Frontier Research Center funded by the U.S. Department of Energy, Office of Science, Basic Energy Sciences under Award No. DE-SC0016574. Work at the University of Tennessee (neutron total scattering analysis) was supported by the U.S. Department of Energy (DOE), Office of Science, Basic Energy Sciences (BES), under Award No. DE-SC0020321. Research at the Spallation Neutron Source (SNS) with the Nanoscale Ordered Materials Diffractometer (NOMAD) at Oak Ridge National Laboratory (ORNL) was supported by the U.S. Department of Energy, Office of Science, Basic Energy Sciences. The heavy Au ion irradiation was conducted at the X0 branch of the UNILAC accelerator of the GSI Helmholtz Center for Heavy Ion Research in Darmstadt, Germany.

References

[1] W. Lutze, R.C. Ewing, Radioactive waste forms for the future, Elsevier Science Pub. Co., Inc, New York, 1988, p. 712.
[2] R. Ewing, W. Weber, F. Clinard Jr, Radiation effects in nuclear waste forms for high-level radioactive waste, Prog. Nucl. Energy 29 (1995) 63–127.
[3] V. Aubin, D. Caurant, D. Gourier, N. Baffier, T. Advocat, F. Bart, G. Leturcq, J.M. Costantini, Synthesis, characterization and study of the radiation effects on hollandite ceramics developed for cesium immobilization, Mater. Res. Soc. Symp. Proc. 807 (2003) 315, doi:10.1557/PROC-807-315.
[4] A. Leinekugel-le-Cocq, P. Deniard, S. Jobic, R. Cerny, F. Bart, H. Emerich, Synthesis and characterization of hollandite-type material intended for the specific containment of radioactive cesium, J. Solid State Chem. 179 (2006) 3196–3208.
[5] M. Carter, E. Vance, H. Li, Hollandite-rich ceramic melts for the immobilisation of Cs, Mater. Res. Soc. Symp. Proc. 807 (2003) 249, doi:10.1557/PROC-807-249.
[6] C. Fillet, T. Advocat, F. Bart, G. Leturcq, H. Rabiller, Titanate-based ceramics for separated long-lived radionuclides, C. R. Chim. 7 (2004) 1165–1172.
[7] M. Zhao, Y. Xu, L. Shuller-Nickles, J. Amoroso, A.I. Frenkel, Y. Li, W. Gong, K. Lilova, A. Navrotsky, K.S. Brinkman, Compositional control of radionuclide retention in hollandite-based ceramic waste forms for Cs-immobilization, J. Am. Ceram. Soc. 102 (2019) 4314–4324.
[8] R. Grote, M. Zhao, L. Shuller-Nickles, J. Amoroso, W. Gong, K. Lilova, A. Navrotsky, M. Tang, K. Brinkman, Compositional control of tunnel features in hollandite-based ceramics: structure and stability of $(Ba,Cs)_{1.33}(Zn,Ti)_8O_{16}$, J. Mater. Sci. 54 (2019) 1112–1125.
[9] H. Xu, L. Wu, J. Zhu, A. Navrotsky, Synthesis, characterization and thermochemistry of Cs-, Rb-and Sr-substituted barium aluminium titanate hollandites, J. Nucl. Mater. 459 (2015) 70–76.
[10] H. Xu, G.C. Costa, C.R. Stanek, A. Navrotsky, Structural behavior of $Ba_{1.24}Al_{2.48}Ti_{5.52}O_{16}$ hollandite at high temperature: an in situ neutron diffraction study, J. Am. Ceram. Soc. 98 (2015) 255–262.
[11] A. Abdelouas, S. Utsunomiya, T. Suzuki, B. Grambow, T. Advocat, F. Bart, R.C. Ewing, Effects of ionizing radiation on the hollandite structure-type: $Ba_{0.85}Cs_{0.26}Al_{1.35}Fe_{0.77}Ti_{5.90}O_{16}$, Am. Mineral 93 (2008) 241–247.
[12] Y. Xu, M. Feygenson, K. Page, L.S. Nickles, K.S. Brinkman, Structural evolution in hollandite solid solutions across the A-site compositional range from $Ba_{1.33}Ga_{2.66}Ti_{5.34}O_{16}$ to $Cs_{1.33}Ga_{1.33}Ti_{6.67}O_{16}$, J. Am. Ceram. Soc. 99 (2016) 4100–4106.

[13] V. Aubin-Chevaldonnet, D. Caurant, A. Dannoux, D. Gourier, T. Charpentier, L. Mazerolles, T. Advocat, Preparation and characterization of $(Ba,Cs)(M,Ti)_8O_{16}$ ($M = Al^{3+}$, Fe^{3+}, Ga^{3+}, Cr^{3+}, Sc^{3+}, Mg^{2+}) hollandite ceramics developed for radioactive cesium immobilization, J. Nucl. Mater 366 (2007) 137–160.

[14] M. Zhao, P. Russell, J. Amoroso, S. Misture, S. Utlak, T. Besmann, L. Shuller-Nickles, K.S. Brinkman, Exploring the links between crystal chemistry, cesium retention, thermochemistry and chemical durability in single-phase $(Ba,Cs)_{1.33}(Fe,Ti)_8O_{16}$ hollandite, J. Mater. Sci. 55 (2020) 6401–6416.

[15] S. Kesson, T. White, Radius ratio tolerance factors and the stability of hollandites, J. Solid State Chem. 63 (1986) 122–125.

[16] J. Zhang, C.W. Burnham, Hollandite-type phases: geometric consideration of unit-cell size and symmetry, Am. Mineral. 79 (1994) 168–174.

[17] R. Grote, T. Hong, L. Shuller-Nickles, J. Amoroso, M. Tang, K. Brinkman, Radiation tolerant ceramics for nuclear waste immobilization: Structure and stability of cesium containing hollandite of the form $(Ba,Cs)_{1.33}(Zn,Ti)_8O_{16}$ and $(Ba,Cs)_{1.33}(Ga,Ti)_8O_{16}$, J. Nucl. Mater. 518 (2019) 166–176.

[18] W. Weber, R. Ewing, C. Catlow, T.D. De La Rubia, L. Hobbs, C. Kinoshita, H. Matzke, A.T. Motta, M. Nastasi, E. Salje, Radiation effects in crystalline ceramics for the immobilization of high-level nuclear waste and plutonium, J. Mater. Res. 13 (1998) 1434–1484.

[19] H. Matzke, Radiation damage in crystalline insulators, oxides and ceramic nuclear fuels, Radiat. Eff. 64 (1982) 3–33.

[20] M. Tang, P. Tumurugoti, B. Clark, S. Sundaram, J. Amoroso, J. Marra, C. Sun, P. Lu, Y. Wang, Y.-B. Jiang, Heavy ion irradiations on synthetic hollandite-type materials: $Ba_{1.0}Cs_{0.3}A_{2.3}Ti_{5.7}O_{16}$ (A= Cr, Fe, Al), J. Solid State Chem. 239 (2016) 58–63.

[21] J. Woolfrey, K. Reeve, D. Cassidy, Accelerated irradiation testing of SYNROC and its constituent minerals using fast neutrons, J. Nucl. Mater. 108 (1982) 739–747.

[22] R.I. Palomares, J. Shamblin, C.L. Tracy, J. Neuefeind, R.C. Ewing, C. Trautmann, M. Lang, Defect accumulation in swift heavy ion-irradiated CeO_2 and ThO_2, J. Mater. Chem. A 5 (2017) 12193–12201.

[23] M. Lang, E.C. O'Quinn, J. Shamblin, J. Neuefeind, Advanced Experimental Technique for Radiation Damage Effects in Nuclear Waste Forms: Neutron Total Scattering Analysis, MRS Adv 3 (2018) 1735–1747.

[24] C.-K. Chung, J. Shamblin, E.C. O'Quinn, A. Shelyug, I. Gussev, M. Lang, A. Navrotsky, Thermodynamic and structural evolution of $Dy_2Ti_2O_7$ pyrochlore after swift heavy ion irradiation, Acta Mater 145 (2018) 227–234.

[25] J.F. Ziegler, M.D. Ziegler, J.P. Biersack, SRIM–The stopping and range of ions in matter (2010), Nucl. Instrum. Meth. B 268 (2010) 1818–1823.

[26] J. Shamblin, C.L. Tracy, R.I. Palomares, E.C. O'Quinn, R.C. Ewing, J. Neuefeind, M. Feygenson, J. Behrens, C. Trautmann, M. Lang, Similar local order in disordered fluorite and aperiodic pyrochlore structures, Acta Mater 144 (2018) 60–67.

[27] J. Neuefeind, M. Feygenson, J. Carruth, R. Hoffmann, K.K. Chipley, The nanoscale ordered materials diffractometer NOMAD at the spallation neutron source SNS, Nucl. Instrum. Meth. B 287 (2012) 68–75.

[28] A.C. Larson, R.B. Von Dreele, General Structure Analysis System (GSAS), Report LAUR 86-748, Los Alamos National Laboratory, Los Alamos, NM, 2000.

[29] C. Farrow, P. Juhas, J. Liu, D. Bryndin, E. Božin, J. Bloch, T. Proffen, S. Billinge, PDFfit2 and PDFgui: computer programs for studying nanostructure in crystals, J. Phys. Condens. Matter 19 (2007) 335219.

[30] K. Momma, F. Izumi, VESTA 3 for three-dimensional visualization of crystal, volumetric and morphology data, J. Appl. Crystallogr. 44 (2011) 1272–1276.

[31] A. Navrotsky, Progress and new directions in high temperature calorimetry revisited, Phys. Chem. Miner. 24 (3) (1997) 222–241.

[32] A. Navrotsky, Progress and new directions in calorimetry: A 2014 perspective, J. Am. Ceram. Soc. 97 (2014) 3349–3359.

[33] S. Hayun, T.B. Tran, J. Lian, A.F. Fuentes, A. Navrotsky, Energetics of stepwise disordering transformation in pyrochlores, $RE_2Ti_2O_7$ (RE= Y, Gd and Dy), Acta Mater 60 (2012) 4303–4310.

[34] M. Ishii, Y. Fujiki, T. Ohsaka, Raman scattering in one-dimensional ionic conductors Rb-priderites, Solid State Commun 55 (1985) 1123–1126.

[35] T. Ohsaka, Y. Fujiki, Raman spectra in hollandite type compounds $K_{1.6}Mg_{0.8}Ti_{7.2}O_{16}$ and $K_{1.6}Al_{1.6}Ti_{6.4}O_{16}$, Solid State Commun. 44 (1982) 1325–1327.

[36] N. Roy, Y. Park, Y. Sohn, K.T. Leung, D. Pradhan, Green synthesis of anatase TiO_2 nanocrystals with diverse shapes and their exposed facets-dependent photoredox activity, ACS Appl. Mater. & Interfaces 6 (2014) 16498–16507.

[37] S. Porto, P. Fleury, T. Damen, Raman spectra of TiO_2, MgF_2, ZnF_2, FeF_2, and MnF_2, Phys. Rev. 154 (1967) 522–526.

[38] Y. Shibata, T. Suemoto, M. Ishigame, Raman scattering studies of mobile ions in superionic conductor hollandites, Phys. Status Solidi B 134 (1986) 71–79.

[39] A.S. Poyraz, J. Huang, C.J. Pelliccione, X. Tong, S. Cheng, L. Wu, Y. Zhu, A.C. Marschilok, K.J. Takeuchi, E.S. Takeuchi, Synthesis of cryptomelane type α-MnO_2 ($KxMn_8O_{16}$) cathode materials with tunable K^+ content: the role of tunnel cation concentration on electrochemistry, J. Mater. Chem. A 5 (2017) 16914–16928.

[40] A. Knyazev, M. Mączka, I. Ladenkov, E. Bulanov, M. Ptak, Crystal structure, spectroscopy, and thermal expansion of compounds in M^I_2O–Al_2O_3–TiO_2 system, J. Solid State Chem. 196 (2012) 110–118.

[41] M. Zhao, J.W. Amoroso, K.M. Fenker, D.P. DiPrete, S. Misture, S. Utlak, T. Besmann, K. Brinkman, The effect of cesium content on the thermodynamic stability and chemical durability of $(Ba,Cs)_{1.33}(Al,Ti)_8O_{16}$ hollandite, J. Am. Ceram. Soc. 103 (2020) 7310–7321.

[42] R.D. Shannon, Revised effective ionic radii and systematic studies of interatomic distances in halides and chalcogenides, Acta Crystallogr. A 32 (1976) 751–767.

[43] E.C. O'Quinn, J. Shamblin, B. Perlov, R.C. Ewing, J. Neuefeind, M. Feygenson, I. Gussev, M. Lang, Inversion in $Mg_{1-x}Ni_xAl_2O_4$ spinel: New insight into local structure, J. Am. Chem. Soc. 139 (2017) 10395–10402.

[44] W. Baur, The geometry of polyhedral distortions. Predictive relationships for the phosphate group, Acta Crystallogr. B 30 (1974) 1195–1215.

[45] L. Pauling, The principles determining the structure of complex ionic crystals, J. Am. Chem. Soc. 51 (1929) 1010–1026.

[46] T. Hartmann, A. Alaniz, F. Poineau, P. Weck, J. Valdez, M. Tang, G. Jarvinen, K. Czerwinski, K. Sickafus, Structure studies on lanthanide technetium pyrochlores as prospective host phases to immobilize ^{99}technetium and fission lanthanides from effluents of reprocessed used nuclear fuels, J. Nucl. Mater. 411 (2011) 60–71.

[47] W. Zachariasen, The crystal structure of monoclinic metaboric acid, Acta Crystallogr. B 16 (1963) 385–389.

[48] V. Aubin-Chevaldonnet, D. Caurant, D. Gourier, T. Charpentier, S. Esnouf, Synthèse et stabilité sous irradiation électronique d'une céramique $Ba_{1,16}Al_{2,32}Ti_{5,68}O_{16}$ de structure hollandite envisagée pour le confinement de césium radioactif, C. R. Chim. 12 (2009) 1079–1092.

[49] B. Ahmmad, K. Leonard, M.S. Islam, J. Kurawaki, M. Muruganandham, T. Ohkubo, Y. Kuroda, Green synthesis of mesoporous hematite (α-Fe_2O_3) nanoparticles and their photocatalytic activity, Adv. Powder Technol. 24 (2013) 160–167.

[50] D. Tuschel, Selecting an excitation wavelength for Raman spectroscopy, Spectrosc 31 (2016) 14–23.

[51] K. Sikafus, R. Grimes, S. Corish, A. Cleave, M. Tang, C. Stanek, B. Uberuaga, J. Valdez, Layered atom arrangements in complex materials, Report LA-14205, Los Alamos National Laboratory, Los Alamos, NM, 2005.

[52] W. Weber, J. Wald, H. Matzke, Effects of self-radiation damage in Cm-doped $Gd_2Ti_2O_7$ and $CaZrTi_2O_7$, J. Nucl. Mater. 138 (1986) 196–209.

[53] G. Sattonnay, S. Moll, L. Thomé, C. Decorse, C. Legros, P. Simon, J. Jagielski, I. Jozwik, I. Monnet, Phase transformations induced by high electronic excitation in ion-irradiated $Gd_2(Zr_xTi_{1-x})_2O_7$ pyrochlores, J. Appl. Phys. 108 (2010) 103512.

[54] S. Park, M. Lang, C.L. Tracy, J. Zhang, F. Zhang, C. Trautmann, M.D. Rodriguez, P. Kluth, R.C. Ewing, Response of $Gd_2Ti_2O_7$ and $La_2Ti_2O_7$ to swift-heavy ion irradiation and annealing, Acta Mater 93 (2015) 1–11.

[55] G. Sattonnay, N. Sellami, L. Thomé, C. Legros, C. Grygiel, I. Monnet, J. Jagielski, I. Jozwik-Biala, P. Simon, Structural stability of $Nd_2Zr_2O_7$ pyrochlore ion-irradiated in a broad energy range, Acta Mater 61 (2013) 6492–6505.

[56] R. Mouginot, T. Sarikka, M. Heikkilä, M. Ivanchenko, U. Ehrnstén, Y.S. Kim, S.S. Kim, H. Hänninen, Thermal ageing and short-range ordering of Alloy 690 between 350 and 550°C, J. Nucl. Mater. 485 (2017) 56–66.

[57] L. Barnard, G. Young, B. Swoboda, S. Choudhury, A. Van der Ven, D. Morgan, J. Tucker, Atomistic modeling of the order–disorder phase transformation in the Ni_2Cr model alloy, Acta Mater 81 (2014) 258–271.